Available online at www.sciencedirect.com
SCIENCE DIRECT
Polymer 46 (2005) 11019–11034
polymer
www.elsevier.com/locate/polymer

A molecular dynamics study of the effect of ethyl branches on the orthorhombic structure of polyethylene

T.L. Phillips, S. Hanna*

H.H. Wills Physics Department, University of Bristol, Tyndall Avenue, Bristol BS8 1TL, UK

Received 23 March 2005; received in revised form 4 September 2005; accepted 5 September 2005
Available online 27 September 2005

Abstract

Molecular dynamics computer simulations are presented for polyethylene crystals containing ethyl branches. The crystals are simulated using an all-atom (explicit hydrogen) molecular mechanics force field. The effect of the branches in expanding the crystalline unit cell is demonstrated for a range of branch densities. We compare the behaviour of two types of model, each consisting of arrays of 48 chains. In the first, the polyethylene chains are effectively infinite in length, by virtue of the periodic boundary conditions, which link the polymer chains across the faces of the simulation box. In the second model, we simulate long *n*-alkanes. Two different chain lengths are considered, containing 24 or 48 carbon atoms. By examining the individual torsional angles and the setting angles of each segment of each chain, it is possible to demonstrate that branches are incorporated into the unit cell without the introduction of gauche defects in the polymer backbones. The effect of large numbers of branches is to expand the cell to such an extent that a mobile rotator phase is induced i.e. the system forms a dynamic rotationally disordered crystal in which chain sliding occurs readily. Although such high branch densities in the crystalline phase are not accessible experimentally, the prediction of a mesophase is interesting, because it may have implications for crystallisation. For example, the mesophase could occur transiently during crystallisation, as has been suggested for linear chains, and it would fulfil the dual role of allowing the growing crystals to thicken, and providing the branches with the opportunity to diffuse out of the crystal.

Keywords: Branched polyethylene; Computer simulation; Orthorhombic phase

1. Introduction

This paper addresses the influence of short chain branching on the molecular packing in crystals of polyethylene (PE). Many commercial grades of PE contain small proportions of short branches, which are often added to enhance their mechanical properties. Typical branches consist of short linear alkanes, such as methyl, ethyl, butyl or hexyl groups, or branched units such as 4-methyl-1-pentene. The maximum concentration added in commercial formulations is typically around 18 short chain branches per 1000 backbone carbons (18 SCB/1000C).

There has been much debate as to where, within semicrystalline polymers, short chain branches are likely to be found. On the basis of equilibrium thermodynamics, for example, it might be argued that the branches should be rejected from the crystalline regions during crystallisation, as they represent a type of defect that would increase the internal energy of the crystal. On the other hand, the kinetics of crystallisation are such that it is likely some of the branches will be trapped within the crystals, suggesting a degree of partial segregation [1,2].

There have been many experimental studies on short-chain-branched systems, principally using either X-ray diffraction or solid state ^{13}C nuclear magnetic resonance (NMR) spectroscopy. The general observation from X-ray studies is that the *a* and *b* parameters of the orthorhombic unit cell of PE both increase as the branch content increases [3–13]. Many of the key measurements in this area have been usefully summarised in the paper by Howard and Crist [13]. The natural conclusion from this is that some proportion of the branches sits within the unit cells, pushing the polymer chains apart. However, it has been pointed out that a segregation of the branches to the fold surface could also have this effect on the *a* and *b* parameters [14], as it would result in reduced lamellar thickness which is also known to cause unit cell expansion [15,16]. However, in

* Corresponding author. Tel.: +44 117 928 8771; fax: +44 117 925 5624.
E-mail address: s.hanna@bristol.ac.uk (S. Hanna).

0032-3861/$ - see front matter © 2005 Elsevier Ltd. All rights reserved.
doi:10.1016/j.polymer.2005.09.018

a recent study combining X-ray diffraction and computer modelling, Baker and Windle [17] have concluded that the observed intensities of the crystalline diffraction peaks from short-chain-branched systems are inconsistent with branch exclusion, and in general agreement with branch inclusion models, for a range of different branch types.

NMR studies provide additional evidence for the disposition of the branches, and are able to provide quantitative figures for the proportion of branches within the crystals. The results require some interpretation, however, and can lead to conflicting conclusions. For example, some workers [18,19] have suggested that chain branches of $-C_2H_5$ and above are excluded from the crystal lattice, being found, instead, either in an interfacial region or within amorphous, non-crystalline regions.

The NMR definition of the interfacial region is based upon the mobility of carbon atoms. When estimates of crystallinity, determined by various methods, are compared, the sum of the crystalline and (NMR) interfacial regions are similar to the estimated crystalline component as determined by X-ray diffraction [20]. This means that it is possible for the NMR-defined interfacial-region to be made up of *trans* chain segments that would contribute to crystalline diffraction patterns, while lacking the tight packing and high degree of order that are required to contribute significantly to NMR estimates of crystallinity.

With this caveat, Pérez and co-workers have concluded that ethyl branches are included within the crystalline phase, to a limited extent, and have reported on two ethyl-branched PE samples with overall branch compositions of 17 SCB/1000C and 21 SCB/1000C, which appear to contain crystalline branch compositions of 2.7 and 6.1 SCB/1000C, respectively [21,22]. The general consensus now appears to be that methyl branches are readily tolerated within PE crystals, ethyl branches are included to a lesser extent, and longer branches are generally rejected.

If we accept that methyl and ethyl branches may be incorporated into the PE crystal structure, the question must be: how can they fit into what is already a close-packed structure? Napolitano et al. [23] performed molecular mechanics calculations on isolated PE chains containing a single methyl or ethyl branch. They concluded that the lowest energy state would consist of the branch being perpendicular to the backbone. In the case of the ethyl branch, this led to significant lattice strain when the chains were packed in a unit cell. Baker and Windle [17] however, showed that the packing constraints would be less severe, if the branch adopted a higher energy conformation, and was allowed to turn to lie parallel with the backbones. Using molecular mechanics, they examined several models, consisting of blocks of $2\times3\times13$ unit cells of PE and containing branches of varying lengths. They showed how, in each case, distortions extended over several unit cells in each direction to permit the branches to be accommodated. Lattice expansion was not simulated directly; rather, the cell parameters were set according to the experimentally determined parameters for the sample under examination.

The work presented in the current paper extends the molecular modelling of Baker and Windle [17], by applying molecular dynamics methods to the problem. Our study aims to investigate the effects of short chain branches on the local crystal environment and unit cell parameters. In particular, we will examine the effects of branching on the crystal packing and chain mobility, and on the conformations of the chains in the vicinity of the branch point. In addition, we will use our model to explore the limits of branching that the PE crystal can support, and show the effect that different types of computer model will have on the predicted behaviour of the PE chains.

2. Computer models

The problem of finding a reliable computer model for PE has been discussed in a previous paper [24]. The main difficulty is that PE crystals are poorly ordered, and the crystal structure appears to be influenced by the presence of fold surfaces, making it challenging to create a model that is small enough to be computationally feasible, but large enough that it is representative of the structure as a whole. It is common practice to employ periodic boundary conditions in such models. However, while these make the simulation box more representative of the bulk of a large crystal, they have the disadvantage that they eliminate the possibility of incorporating chain folds, unless the simulation box is very large indeed. Therefore, any computer model is necessarily an approximation—the two commonest approaches are to use straight finite *n*-alkane chains, of length equivalent to one side of the simulation box, or to use infinite chains, created by bonding each chain across the face of the simulation box to a periodic image of itself. We also discussed a third type of model, which was based on jog-defects, and designed to mimic the effect of chain-folds, in our previous paper.

As mentioned in Section 1, the aim of this investigation is to examine the local effects that ethyl branches have on computer models of crystalline polyethylene-like materials. To this end, both infinite and finite chain models have been used, all models consisting of 48 chain stems arranged in an array of 4×6 unit cells, as depicted in Fig. 1. Details of the models are given in Table 1.

The infinite models have the benefit of not containing chain ends or conformational defects and as such provide an idealised environment. However, this is an environment that also has significant limitations. Most notable is the impossibility for one chain to contract relative to the other chains in the simulation box. In a real system, we would expect this to be possible, by virtue of the presence of chain ends and other defects. For this reason, although we will examine the effect of including a single branch in infinite chain models, the effect of increasing branch content will be examined mainly using finite chain models. Although the finite chain models are effectively *n*-alkanes with occasional branches, we will regard them, here, as a model system for PE.

Two infinite chain models were built containing $4\times6\times12$ unit cells and $4\times6\times24$ unit cells of PE i.e. chain stems consisting of $-C_{24}H_{48}-$ and $-C_{48}H_{96}-$, respectively. Model

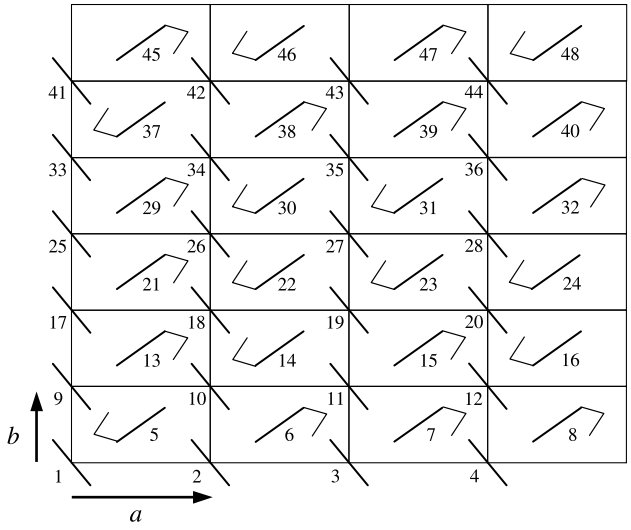

Fig. 1. A projection of the starting configuration of the models. The heavy line segments represent the projections of the planar zig-zags of the polymer backbones. The lighter, bent, segments indicate the possible locations of branches. Only the chains at the centre of each unit cell are able to be branched; when present, the branch will be on the side of the chain indicated.

structures were constructed in both branched and unbranched forms to facilitate a comparison. The branched models contained a single $-C_2H_5$ branch located at the mid-point of chain 23 (see Fig. 1).

In the finite chain models, the stems consist either of $C_{24}H_{50}$ or $C_{48}H_{98}$ molecules. Each molecule was randomly displaced in the z direction by an integer number of unit cell repeats. This approach allows for individual chain contraction while avoiding the effects of chain tilting and the co-operative ordering of chain ends, that often occurs if the molecules are arranged in layers [25].

In building the branched finite chain models, attempts were made to avoid overly-systematic defect structures that might distort the results. However, because of the small model size, a certain regularity in defect arrangement would appear to be inevitable. The effect is most pronounced in the model with 24 branches, where every other chain contains a branch.

With this caveat in mind, six finite chain models were built with increasing branch densities. Each model consisted of 4×6 unit cells, each containing a pair of $C_{48}H_{98}$ molecules. Ethyl branches were attached at the mid-point of a random selection of the chains, which in all cases included chain 23 in order to simplify comparisons between the models. The branches were only added to the chains in the centres of each unit cell, in the initial herringbone configuration i.e. the chains with negative setting angles (Fig. 1). Half of these chains were then selected at random and rotated by 180° about the chain axis, after which they were displaced by $c/2$ in the chain axis direction, to restore the crystallographic register of the chains.

Restricting the branches to half of the chains has a particular advantage in avoiding branch–branch interactions, which could have a significant effect in a model of this size. To increase the branch density further the length of the chains was reduced, to $C_{24}H_{50}$, while maintaining the positioning of the 24 branches. This provided a means of increasing the branch density while continuing to avoid branch–branch interactions.

The branch density of each model, calculated as the number of short chain branches per thousand carbon atoms, is shown in Table 1. The highest branch concentration investigated here is 20.8 SCB/1000C, which corresponds to the $4\times6\times C_{24}$ model containing 24 branches.

The branch densities utilised in these simulations are comparable with those found in linear low-density PE (LLDPE) crystals. For example, as mentioned in Section 1, Pérez et al. [21,22] have reported finding ethyl branch densities of 2.7 and 6.1 SCB/1000C within the crystalline phases of two branched PE samples, using ^{13}C NMR.

3. Simulation method

Many of the methods used in this work have been described in detail elsewhere [24]. Here, only a brief outline will be given.

3.1. Model construction

Models were constructed using the lattice parameters ($a=0.740$ nm, $b=0.493$ nm, $c=0.2534$ nm) and carbon atom coordinates given for the PE unit cell by Bunn [26]. The positions of the hydrogen atoms were determined by

Table 1
A summary of the model types and compositions used in the current study

Model	Chain type	Branch number	Branch content (SCB/1000C)	Number of atoms	Equilibration period (ps)	Production period (ps)
$4\times6\times12$ (infinite)	$-C_{24}H_{48}-$	0	0	3456	200	50
		1	0.87	3462	200	50
$4\times6\times24$ (infinite)	$-C_{48}H_{96}-$	0	0	6912	200	50
		1	0.43	6918	200	50
$4\times6\times C_{48}$ (finite)	$C_{48}H_{98}$	0	0	7008	200	50
		1	0.43	7014	200	50
		3	2.60	7026	200	50
		6	5.21	7044	200	50
		12	10.4	7080	200	50
		24	20.8	7152	200	50
$4\times6\times$C24 (finite)	$C_{24}H_{50}$	0	0	3552	200	50
		24	20.8	3196	200	50

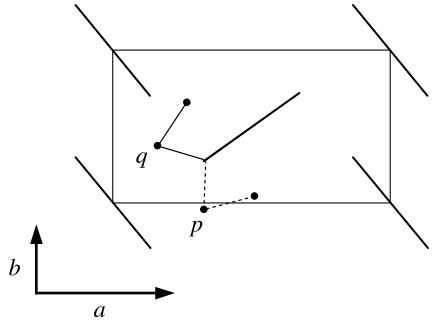

Fig. 2. A projection of one unit cell of polyethylene, showing the two possible branch locations (labelled p and q). Location q is preferred on energetic grounds (see text).

minimising the potential energies of the completed models. The infinite chain models were constructed by replication of the Bunn cell parallel to the coordinate axes. The finite chain models were constructed from the infinite chain models, by cutting the bonds across the (001) face of the simulation box, expanding the box slightly, and adding hydrogen atoms to the terminal CH_2 groups. Each chain was translated by a random number of unit cell repeats parallel to the c axis, and the energy of the whole model was then minimised using molecular mechanics.

The positioning of the branches within each crystallographic unit cell, followed the approach of previous workers [27,28,17] in attaching the branch at the point where there was the most free-volume in the low-energy crystal structure. For methyl branches, there are two possible configurations within the unit cell, labelled p and q in Fig. 2. According to Farmer and Eby [27,28], a methyl at the q position is slightly lower in energy than one at the p position. Accordingly, we adopted the same strategy, adding the first carbon of the side chain at position q, followed by the terminal $-CH_3$ group, turned slightly to bring the ethyl group towards a parallel configuration with the backbone. The energy of the simulation box was then minimised again using molecular mechanics, prior to commencing the molecular dynamics simulations. Since the branches were added at the chain mid-points, and the chains were translated by random distances, it is possible to minimise any interference between side-branches on chains in adjacent unit cells.

For the $4\times6\times24$ and $4\times6\times C_{48}$ models, the dimensions of the simulation box were approximately $30\times30\times60$ Å at ambient temperature and pressure. The $4\times6\times12$ and $4\times6\times C_{24}$ models were approximately half as long, at $30\times30\times30$ Å.

3.2. Molecular dynamics method

Molecular dynamics simulations were performed using the DL_POLY_2 molecular dynamics code from the CCLRC [29], running on a four processor Silicon Graphics Origin 200 computer. All models were equilibrated for 200 ps at 300 K and ambient pressure using the Berendsen integration method [30]. A production period of 50 ps in the microcanonical ensemble was then used to sample the dynamics of each system. A 1 fs time-step was used throughout.

The Berendsen approach to isobaric–isothermal simulation was preferred over the Nosé–Hoover method [31,32] for equilibration, due to its greater efficiency at redistributing thermal energy between the different vibrational modes of the system. This was a particular issue due to the anisotropic nature of the PE crystal. However, because the Berendsen method does not correctly sample the isobaric–isothermal (constant NPT) ensemble, all sampling during the production runs was performed in the microcanonical (constant NVE) ensemble.

The Berendsen method has two parameters, τ_T and τ_P, to control the coupling of the system to the temperature and pressure reservoirs. τ_T was set to 0.4 ps as suggested by Berendsen et al. [30]. τ_P was set to 8 ps to reduce the rate of change of the box dimensions. Although this resulted in slower equilibration, it reduced the likelihood of the SHAKE algorithm (needed for constraining bond lengths—see below) from failing. The problem with the SHAKE algorithm was also related to the anisotropic mechanical and thermal properties of the simulation box and its non-cubic shape. For this reason, it was also necessary to limit the aspect ratio of the simulation box to around 2:1.

3.3. Force field

A molecular mechanics force field including explicit hydrogen atoms was chosen, because earlier investigations have indicated that the united atom approximation does not provide a good representation of the crystal structures of the *n*-alkanes [33].

We have used a force field derived by Smith and Yoon [34] for the present study. This force field was chosen because its authors placed a strong emphasis on finding the correct form for the backbone torsional potential, a key factor in reproducing both the static structure and dynamic motion of non-planar chain conformations. In fact, the Smith and Yoon force field was designed for studying amorphous polymers, so it may be expected to provide a good representation of *gauche* defects and chain branches in more regular systems.

The details of our implementation of this force field have been published elsewhere [24]. The van der Waals interaction was represented by an 'Exponential 6' or Buckingham potential. Bond lengths were held constant using the SHAKE algorithm [33,35]. The torsional potential was designed to model the behaviour of *n*-butane: the parameters used yield a *trans-gauche* energy difference of 2.0 kJ mol^{-1}, and a *trans-gauche* barrier of 12.6 kJ mol^{-1}. The *cis* barrier is 20.2 kJ mol^{-1} and the energy barrier for methyl group rotation is 10.9 kJ mol^{-1}.

Although there are other more detailed force fields available for PE, the Smith and Yoon force field was chosen for the present work because it provides a useful compromise between accuracy and computational effort for these polyethylene-like systems.

3.4. Analysis of torsions and setting angles

Conformational defects manifest themselves through changes in the torsions and setting angles present in the model. Therefore, we calculate frequency distributions both for the backbone torsions and for the setting angles. Rather than examining the setting angles of the whole chain, we calculate it for sub-units consisting of three consecutive methylene groups or carbon atoms. The setting-angle of this three-methylene segment (3MS) is obtained by projecting the three backbone carbon atoms onto the basal plane of the unit cell (the x–y plane) and taking the angle between the bisector of the projected backbone bonds, and the x-axis, as illustrated in Fig. 3(c). We take the setting angle to be positive when measured in the clockwise sense.

While the angle distributions are very informative, it is also enlightening to study the progress of individual torsional angles and defects. By adapting a method presented by Doherty and Hopfinger [36], it is possible to visualise all of the torsions and setting angles within a chain stem as a function of time, in a two-dimensional map. We plot the position of each torsion or setting angle within the model against the vertical axis and indicate the angle by a block of colour, so that a single vertical line of colours can indicate the angles for the whole chain stem. A succession of such lines can show the evolution of the torsions or setting angles of the whole chain stem with time. The construction of the colour map is illustrated in Fig. 3(a), and the colour table used to represent the angles in Fig. 3(b). The colours have been selected so that they give a clear colour difference between the different conformational states. For the torsional angles, the *trans* conformation is green, while the *gauche*$^+$ and *gauche*$^-$ conformations are blue and red respectively. The transition

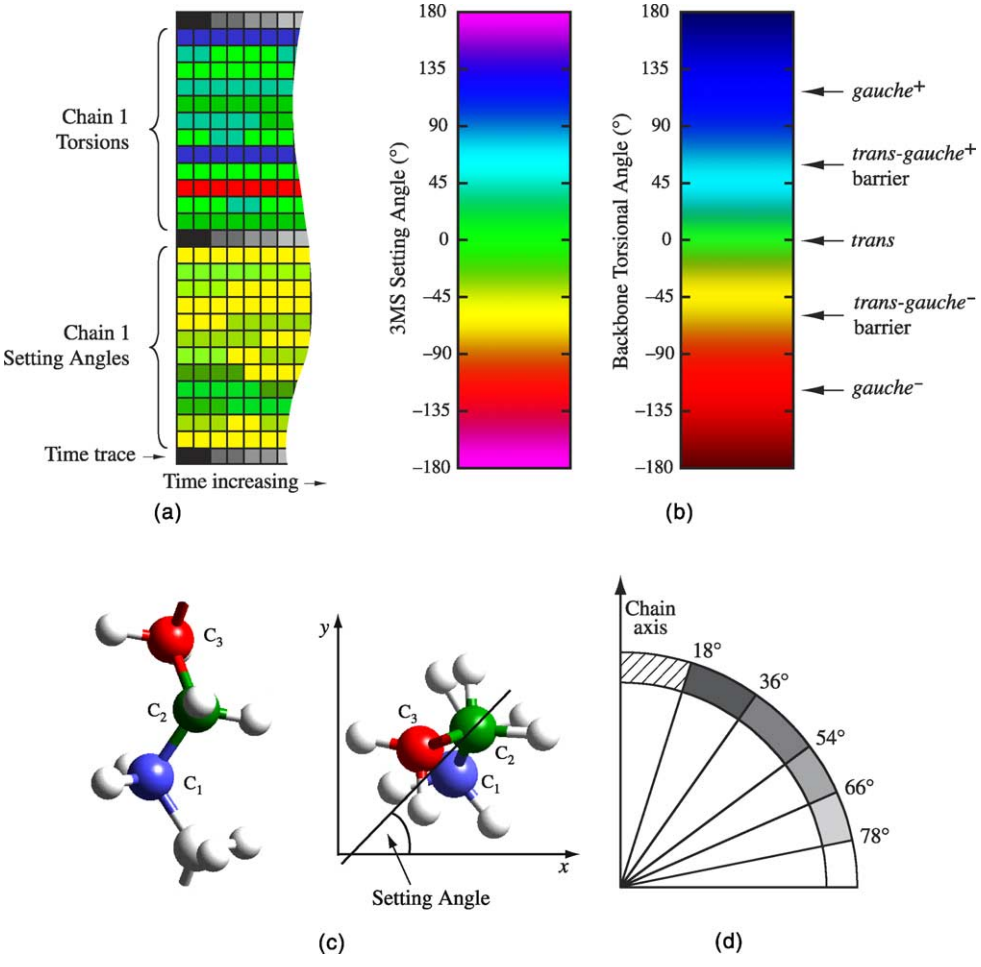

Fig. 3. (a) The method used for displaying torsional angles and three-methylene-segment (3MS) setting angles for a chain stem as a function of time. A vertical column of pixels represents all of the angles within a chain stem at a particular instant in time. The time evolution of a particular angle may be seen by following a horizontal line of colour. The maps also contain time traces, in which each shade of grey represents 2 ps. (b) The colour tables used to represent the setting angles and torsional angles. The setting angle colours are replaced by shades of grey when the 3MS is not aligned to the chain axis, as shown in part (d). (c) Definition of a 3MS setting-angle. The left-hand view shows a short section of polyethylene chain. The co-ordinates of the carbon atoms are projected onto the x–y plane (right hand view) and the setting-angle is defined as the angle between the bisector of the projected C_2–C_1 and C_2–C_3 bonds, and the x-axis. The angle will be taken to be positive when increasing in the clockwise sense. (d) The grey scales associated with the various degrees of 3MS tilt from the chain axis. Segments which are tilted by less than 18° are represented by the colour table shown in (b).

from *trans* to *gauche*$^+$ is achieved via turquoise, while a similar transition to *gauche*$^-$ is via yellow.

The colour table for the 3MS setting-angles has six different colours, each indicating a sixty-degree range. In the event that a 3MS is tilted by more than 18° ($\cos^{-1}$ 0.95) from the average *c*-axis, the calculated setting angle becomes unreliable. In these cases, the coloured pixels are replaced by a grey scale, which is used to indicate the degree of tilt of the 3MS from the chain axis. The shade of grey associated with each range of tilt angles is indicated in Fig. 3(d).

4. Results

4.1. Crystal packing

The influence of ethyl chain branching on the lateral packing of chains in the PE unit cell is shown in Fig. 4. This shows the variation in the *a* and *b* cell parameters as a function of branch density for all of the models. A similar plot of the unit cell density is shown in Fig. 5.

The densities of the models are quite revealing (Fig. 5). Both of the infinite chain models are significantly denser than the experimentally determined crystal density of 1 g/cm^3. This is due to the underestimation of the *b* cell parameter that is most likely an artefact of the force field. A similar effect was observed in simulations of linear PE using the same force field, which were published recently [24]. However, the introduction of chain ends within the body of the crystal reduces the density of the crystals towards the experimental value.

Introducing branches into the models clearly increases the *a* parameter of the unit cell. The effect of a single branch upon *a* is most pronounced (a 3% increase) for the infinite chain model with the shorter repeat (4×6×12). For the infinite chain model with the longer repeat (4×6×24), the increase in *a* is an order of magnitude smaller (0.3%) and there are comparable percentage changes in the densities of the two systems, since the *b* parameter is hardly changed.

In the smaller infinite chain model there is little scope for the chains to deform around a defect, as a consequence of the periodic nature of the chain backbones. Any local deformation can only extend to six unit cells along the chain to either side of the defect, before the structure repeats. This results in a significant strain, which the bond angles cannot support. The only way to reduce the strain is for the whole molecule to move, resulting in expansion of the whole structure. With a longer periodic repeat, there is more opportunity to relieve the strain through small adjustments of the bond angles, and large chain-stem displacements are not required. Hence the overall expansion of the cell is less.

The effect of introducing the chain ends (for example 4×6×C_{48} compared to 4×6×24) is to increase the cell parameter *a*, by about 2%, and reduce the cell density by a similar amount. In fact, there is a large reduction in density (~13%) of the simulation box as a whole, but the value we plot is calculated on the basis of the unit cell parameters rather than the box size, and gives a better indication of the change in packing efficiency. The introduction of a single branch

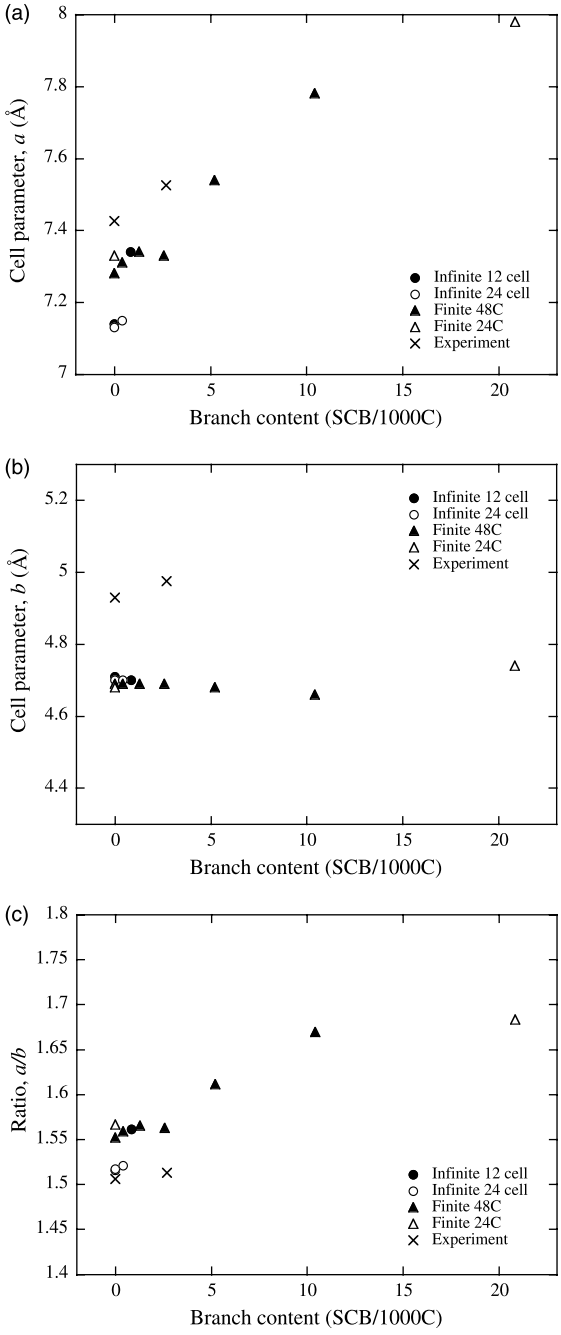

Fig. 4. The basal unit cell dimensions determined from the finite and infinite chain simulations at 300 K. (a) the *a* parameter, (b) the *b* parameter and (c) the ratio *a*/*b*. In all cases the error bars are smaller than the symbols plotted. Limited experimental data points are also shown [21,13].

increases the *a* dimension further, by another 0.4%. This is a smaller effect than is seen for the 4×6×12 infinite chain model but greater than for the 4×6×24 model.

Increasing the branch content of the finite chain model increases the *a* dimension further, and gradually decreases the density. An inspection of the ratio *a*/*b* (Fig. 4(c)) shows that the shape of the cell is moving towards hexagonal, although the ideal ratio of $\sqrt{3}$ is not reached. The model containing six branches (2.6 SCB/1000C) is an exception to this trend. Examination of this model revealed that one of the branches

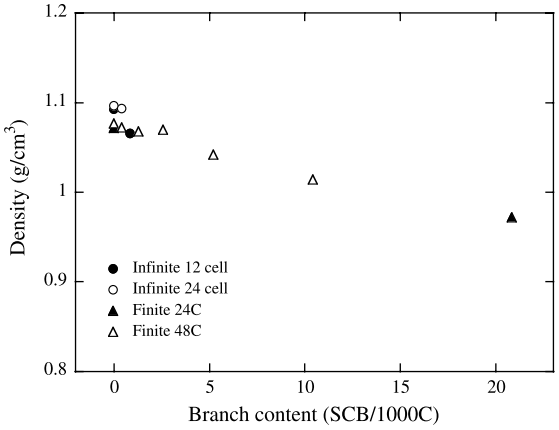

Fig. 5. The unit cell density obtained from the finite and infinite chain simulations at 300 K.

(attached to Chain 29) had interdigitated into the gap between the chain ends of a neighbouring chain (Chain 34). However, it would seem unlikely that this, alone, can account for the increase in density that is seen compared to the model containing 3 branches. We must, therefore, attribute this behaviour to the natural variations that will occur in such a small system with a random arrangement of branches. Such variations may be reduced in future work by using larger models, or multiple models with branches on different sets of chains.

The final increase in branch density, achieved by using shorter finite chains, produces an increase in both a and b, while only slightly changing the ratio a/b, which still remains less than the value needed for a hexagonal phase ($\sqrt{3}$).

4.2. Distribution of angles

The torsional angle distributions for the infinite and finite chain models are shown in Fig. 6. For the infinite chain models, the distributions are entirely made up of *trans* conformations. There are no discernible differences between the unbranched chains of different lengths. However, the introduction of a single branched chain does produce a very slight broadening of the distribution for the $4\times6\times12$ model. Similarly, the 3MS setting angle distributions for the infinite systems (Fig. 7(a)) show two strong peaks at close to $\pm45°$, and it is only the branched $4\times6\times12$ model which shows any noticeable broadening, which must be a consequence of the level of strain present in this system.

The distributions of torsional angles for the finite models (Fig. 6(b)) reveal the effect that branches have on the chain conformations. For the first three branch contents (one, three, and six branches, i.e. up to 2.6 SCB/1000C) the distributions of the torsional angles are almost indistinguishable from the distribution for the unbranched model. However, the next two increments in branch content produce a noticeable broadening

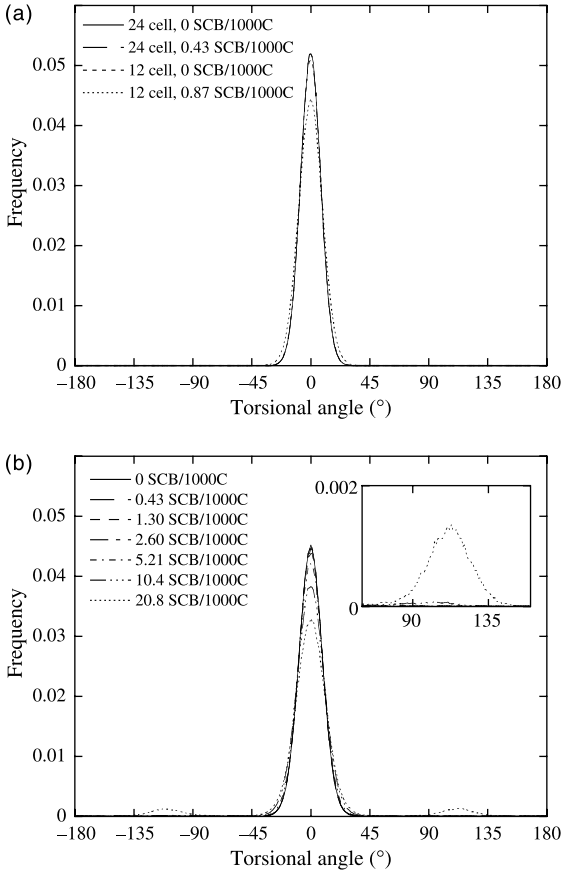

Fig. 6. The distribution of torsional angles for (a) the infinite chain models and (b) the finite chain models, at 300 K.

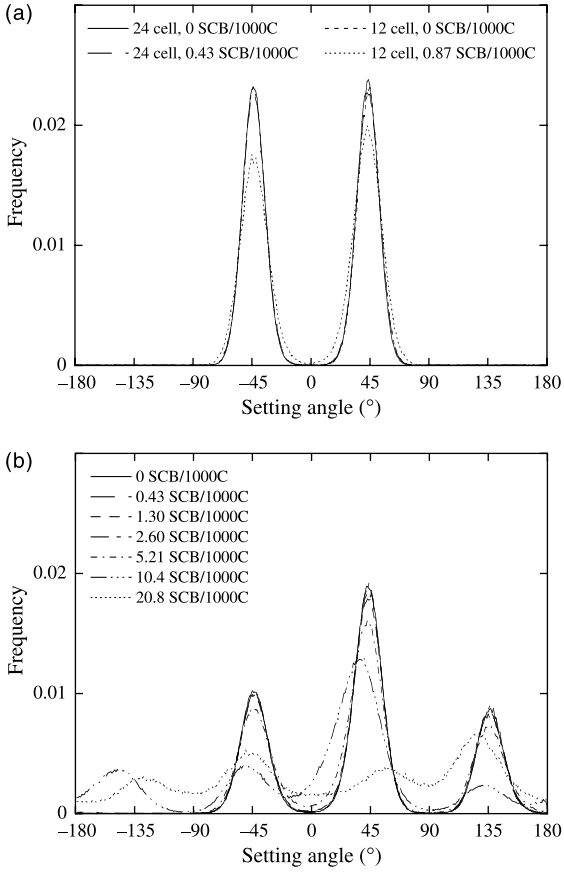

Fig. 7. The distribution of 3MS setting angles (as defined in section 3.4.) for (a) the infinite chain models and (b) the finite chain models, at 300 K.

of the torsional angle distribution. In the case of the 10.4 SCB/1000C system, a very small fraction of *gauche* states become visible (see inset to Fig. 6(b)). However, with the increase to 20.8 SCB/1000C, significant proportions of *gauche* defects become visible.

Since each of the increases in the width of the torsional angle distributions correspond to an increase in a, it may be inferred that the increased free-volume resulting from the presence of branches, leads to an increased range of the librations within the *trans* potential wells, which in turn leads to the formation of *gauche* defects at the highest degrees of branching. The effect of a single branch in the short infinite chain model is stronger than in the finite chain model which is also consistent with the changes in the cell parameter a already seen.

The 3MS setting angle distributions for the finite chain systems (Fig. 7(b)) require some explanation. In the finite chain models, half of the chains that were at negative setting angles (the chains in the centres of each cell), have been rotated by 180°. Thus half of the chains that would have been found at setting-angles of around −45°, can be found at setting-angles close to 135°. Therefore the initial distribution has a single large peak at 45°, and two half-height peaks at −45 and 135°.

This overall shape, corresponding to herringbone packing, persists up to the inclusion of twelve ethyl branches (5.21 SCB/1000C), albeit with some slight broadening. During the equilibration run for the 10.4 SCB/1000C model, some of the chains take up large negative setting-angles, corresponding to 180° rotations about the chain axis. The distribution now contains four peaks but overall appears less symmetrical, with systematic shifts in the average setting angles. At 20.8 SCB/1000C, the setting angle distribution still has four peaks, but now there is evidence for considerable rotational disorder, as 3MS's can be found at all possible setting angles in significant amounts.

4.3. Spatial distribution functions

Spatial distribution functions were calculated for the 3MS units, by taking the centre-of-mass of each 3MS in turn as an origin, and measuring the distances to the centres-of-mass of each of the other 3MS's. The distributions were averaged over all sampled configurations for each simulation. The distributions so obtained for the infinite chain systems, whether branched or unbranched, show the characteristic sharp peaks expected for a crystal and are not shown here. However, in the case of the finite chain systems, some differences are seen with increasing branch content (see Fig. 8).

The projections of the 3MS spatial distributions on to the x–y plane (Fig. 8(a)) show a gradual increase in the breadth of each peak as the branch content increases. This is most noticeable for the $4\times6\times C_{48}$ system with 10.4 SCB/1000C and the $4\times6\times C_{24}$ system with 20.8 SCB/1000C. The biggest differences, however, are observed in the projections on to the plane of the [110] and c axis (Fig. 8(b)). Here it is apparent that, as the level of branching increases the distributions spread in the [110] direction, both in position and width, while remaining relatively constrained in the z-axis direction.

Not only are the distributions spreading in the [110] direction, but there are a small number of interstitial occurrences in the chain axis direction in the $4\times6\times C_{48}$ models, visible as small satellite peaks above and below the main peaks in Fig. 8(b). These occurrences indicate that chains occasionally jump parallel to z, by $\sim c/2$. However, it is the 20.8 SCB/1000C $4\times6\times C_{24}$ model that displays the most striking change of behaviour—the discrete spots formerly observed for each nearest neighbour distribution are smeared into a continuum in the chain direction.

The loss of order in the chain axis direction indicates the onset of chain sliding, which is confirmed by a calculated transport coefficient of 0.05 Å^2/ps. However, even with the loss of order in the chain axis direction, there is still a distinct peak in the first nearest neighbour distribution implying that some neighbouring chains retain a degree of registration.

Taken together with the evidence for rotational disorder shown at the end of the previous section, and notwithstanding the fact that the unit cell parameters do not quite correspond to

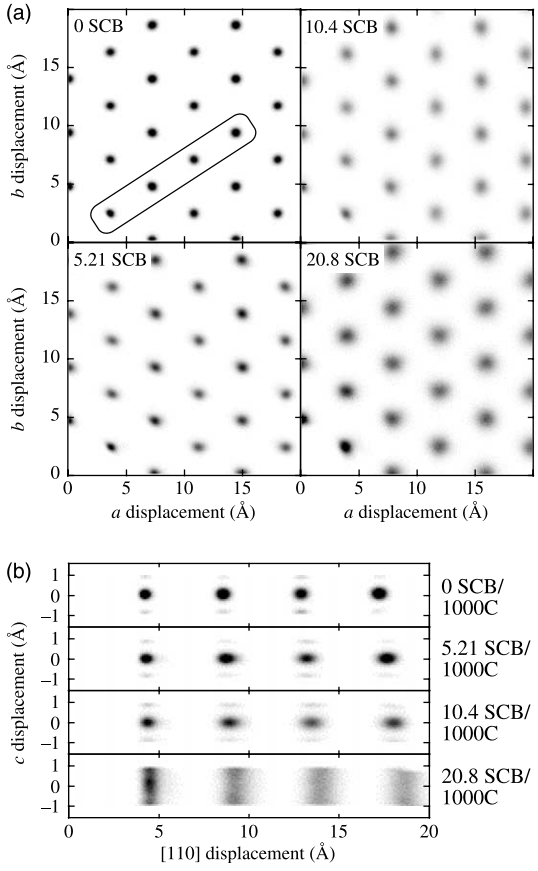

Fig. 8. (a) A plot of the time and space averaged spatial distribution of 3MS in the x–y plane, for a selection of the finite chain ($4\times6\times C_{48}$ and $4\times6\times C_{24}$) branched systems. The marked region indicates the 4 nearest neighbours in the [110] direction, that are also shown in (b). (b) A similar plot for the spatial distribution of 3MS units in a plane containing the [110] lattice vector and the chain axis. N.B. the 20.8 SCB/1000C distribution is relatively weak compared with the other distributions and the grey-scale has been adjusted to make it more visible.

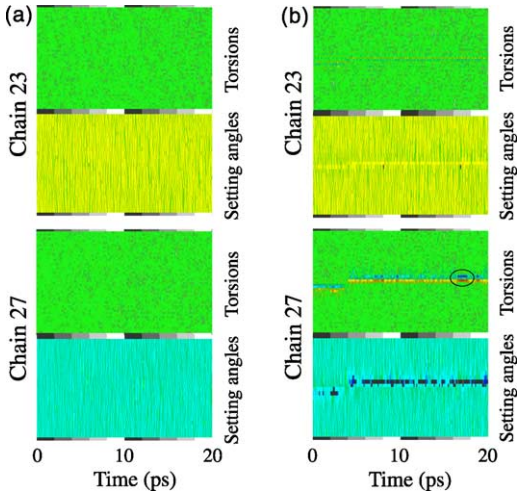

Fig. 9. Colour maps showing the torsional and 3MS setting angles for chains 23 and 27 from (a) the unbranched 4×6×24 model and (b) the same model, containing a single $-C_2H_5$ branch, during the first 20 ps of the 50 ps production run at 300 K. The circled feature is a g^+tg^- defect (see text). The colour table is defined in Fig. 3 and the chain numbers are defined in Fig. 1.

a hexagonal unit cell, the 20.8 SCB/1000C system appears to be displaying the characteristics of a mobile rotator phase, similar to that observed experimentally in shorter *n*-alkanes [37,20] and at elevated temperature and pressure in PE [38–40].

4.4. Behaviour of individual torsions and setting angles

4.4.1. Infinite chain models

The behaviour of particular 3MS's, especially close to branch points or chain ends, is best followed by examining the colour maps described in section 3.4 (see Fig. 3). Fig. 9 shows such maps for two chains taken from the 4×6×24 infinite chain simulations, with and without the presence of a branch. Chains 23 and 27 are shown, because chain 23 contains a branch (in the branched model) and chain 27 is the nearest neighbour to the branch point, as can be seen from Fig. 1.

The colour map of the unbranched infinite model (Fig. 9(a)), is consistent with the herringbone packing of the chains and demonstrates the low level of activity in the torsional angles and 3MS setting-angles, a feature that has already been made clear from the distribution functions. The predominantly yellow colour for the setting angle map for chain 23 indicates a negative setting angle of around −45°, while the cyan colour associated with chain 27 corresponds to a positive setting angle of around +45°. The uniform green of the torsional maps shows that both chains consist entirely of trans conformations.

The introduction of an ethyl branch produces changes in both the branched chain and its nearest neighbour. For chain 23, there is a clear effect in both the torsional and 3MS setting angles indicating the presence of the branch. In the torsional map, the branch causes a slight twisting of the central torsion towards the *trans-gauche*$^-$ barrier. This appears as a feint yellow line across the centre of the plot. The effect is clearer in the setting angle trace: a solid bar of yellow across the plot indicates, in this case, that there is a suppression of the setting angle fluctuations for the 3MS attached to the branch. Surprisingly, the influence of the branch is actually greater on the neighbouring chain, which clearly deforms to accommodate the branch.

In chain 27, throughout the majority of the production run, there is the hint of a g^+tg^- (*gauche*$^+$–*trans*–*gauche*$^-$, sometimes referred to as 2*g*1, or in some texts 2*gl*) defect. This is, again, indicated by the yellow and cyan pixels in the torsional angle colour map, but in this case these occasionally transform to red and blue, when the full g^+tg^- is formed. The longest lived of these is circled. This is a very unusual defect to find in an infinite chain simulation, because it implies a shortening of one chain segment relative to its neighbours, which must be compensated for by a local stretching elsewhere. Such defects do not generally occur spontaneously in infinite chain simulations of unbranched PE, even at 400 K [24]. The 3MS setting angle colour map shows that the formation of this partial, strained defect involves the tilting of one or more 3MS's away from alignment with the chain axis (shown as dark grey pixels).

4.4.2. Finite chain models

As with the infinite chain models, we will focus most attention on chains 23 and 27. The colour maps for the unbranched finite chain model (Fig. 10) usefully show the starting configuration of the model; the chain setting angles are again consistent with herringbone packing. However, this time the setting angle distribution for chain 23 is coloured dark blue, rather than yellow as previously, because this is one of the random set of chains that has been rotated by 180° (see Section 2). As noted above, the inclusion of up to six branches in the finite chain model has little effect on the setting angle distribution. For this reason, only the models containing six or more branches will be considered.

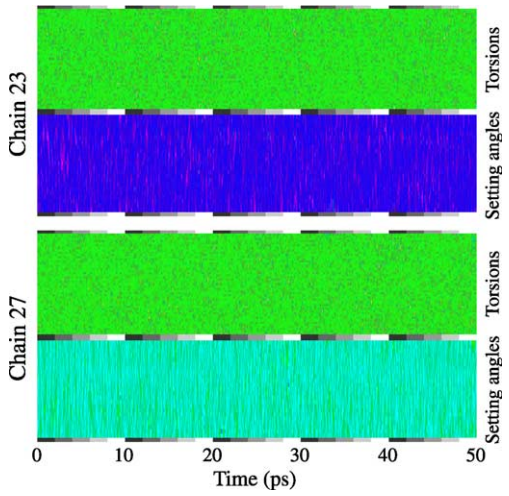

Fig. 10. The colour maps for the torsions and 3MS setting angles for chains 23 and 27 taken from the 4×6×C_{48} unbranched model during the 50 ps production run at 300 K. The colour table is defined in Fig. 3 and the chain numbers are defined in Fig. 1.

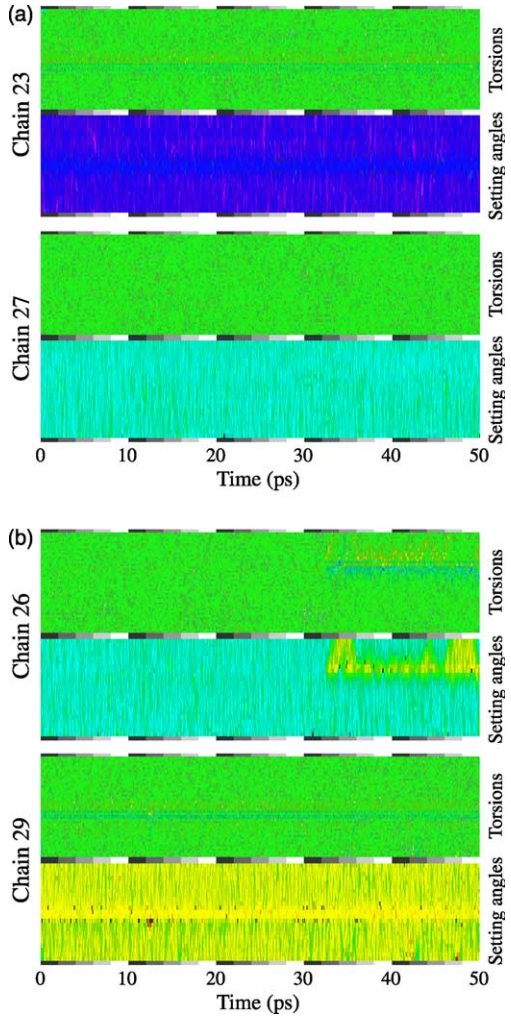

Fig. 11. The colour maps for the torsions and 3MS setting angles for two pairs of chains from the $4\times6\times C_{48}$ model with six ethyl branches (2.6 SCB/1000C) during the 50 ps production run at 300 K. (a) Chains 23 and 27; (b) chains 26 and 29. Chains 23 and 29 contain branches, whereas chains 27 and 26, respectively are the unbranched nearest neighbours. The positions of the chains within the model are given in Fig. 1, and the colour table is defined in Fig. 3.

Whereas, in the infinite chain models the effect of branching was seen most strongly in the neighbouring chain closest to the branch, the same is not the case for the finite chain models. In fact, the influence of chain branches on the conformations of adjacent molecules is barely discernible in the finite chain case. For example, Fig. 11 shows two pairs of chains taken from the model containing six branches (2.6 SCB/1000C). The branched chains are numbers 23 and 29, and the main influence of the branch is seen as a suppression in fluctuation of the setting angles adjacent to the branch. There are also a number of 3MS's close to the branch that are tilted away from the chain axis. These appear as occasional dark grey pixels. The unbranched chain adjacent to chain 23 (chain 27, Fig. 11(a)) is devoid of interest, displaying no deviation from all-*trans* conformations and uniform setting angles. However, the neighbouring chain to chain 29 (chain 26, Fig. 11(b)) shows an intriguing effect, which is reproduced in other chain pairs that are not shown here. For the first part of the simulation, chain 26 appears unaffected by the nearby branch. Then, after 32 ps, the upper part of the chain, that which is above the branch point of chain 29, twists from a positive setting angle (cyan) towards a negative setting angle (yellow). The twisting appears to start opposite the branch and propagate towards the chain end. The twisting is also visible to a lesser extent, in the torsional map for chain 26. It does not, however, lead to the formation of any *gauche* defects.

Fig. 12 shows the effect of adding further branches to the model. The model containing twelve branches (5.21 SCB/1000C, Fig. 12(a)) displays an increase in the fluctuation amplitude for the setting angles, as witnessed by the greater range of colours present in the setting angle map for the branched chain. Occasional brief g^+tg^- defects are also observed, one of which is circled. In other respects, the simulation appears to be very similar to the 2.6 SCB/1000C example.

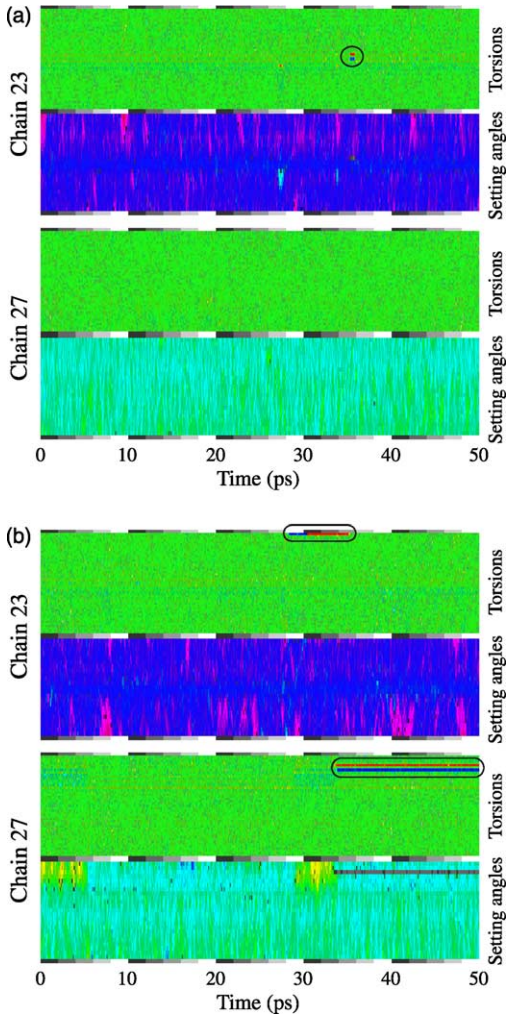

Fig. 12. The colour maps for the torsions and 3MS setting angles for chains 23 and 27 from the $4\times6\times C_{48}$ model, containing (a) twelve ethyl branches (5.21 SCB/1000C) and (b) twenty-four ethyl branches (10.4 SCB/1000C) during the 50 ps production run at 300 K. The highlighted regions contain g^+tg^- and chain-end *gauche* states. The colour table is defined in Fig. 3 and the chain numbers are defined in Fig. 1.

The inclusion of 24 branches (10.4 SCB/1000C, Fig. 12(b)) in the model has a significant effect. It appears that the extra free volume in the simulation box, resulting from the large number of branches, is enabling the backbones of the molecules to become more disordered. This is manifested by an increase in the range and duration of setting angle fluctuations, in both of the chains shown. The fluctuations appear to be initiated both adjacent to the branches, and at the chain ends, and are seen to propagate rapidly along the chains. The increase in disorder is also indicated by the presence of *gauche* defects. For example, a long duration g^+tg^- defect is highlighted in chain 27, and a chain-end *gauche* defect is similarly marked in chain 23.

This trend continues when we look at the $4\times6\times C_{24}$ model with 24 branches (20.8 SCB/1000C). It has already been established that this model appears to display a mobile rotator phase. The colour maps further support this classification, and

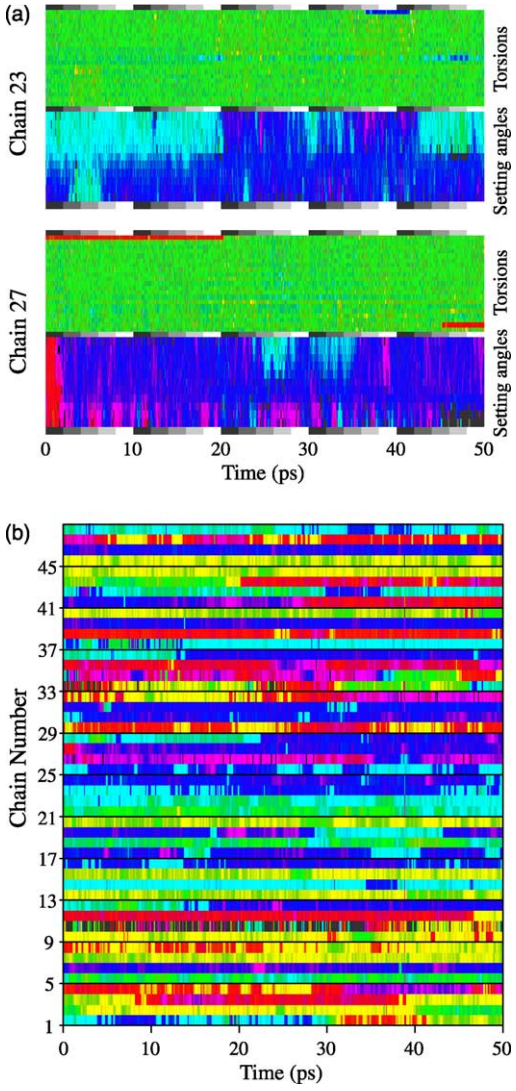

Fig. 13. (a) The colour maps for the torsions and 3MS setting angles for chains 23 and 27 and (b) the setting angles averaged over each chain, for the whole of the twenty-four branch $4\times6\times C_{24}$ model (20.8 SCB/1000C), f or the duration of the 50 ps production run at 300 K. The colour table is defined in Fig. 3 and the chain numbers are defined in Fig. 1.

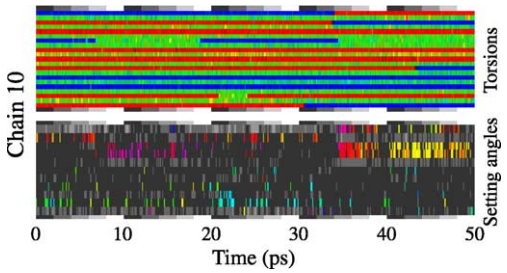

Fig. 14. The colour maps for the torsions and 3MS setting angles for chain 10 from the same model as Fig. 13 (20.8 SCB/1000C). The chain has collapsed with the formation of multiple *gauche* defects. The colour table is defined in Fig. 3 and the chain numbers are defined in Fig. 1.

confirm that the rotational disorder is, indeed, dynamic. Fig. 13(a) once again shows the behaviour of chains 23 (branched) and 27 (unbranched) in the model. The chains show frequent and prolonged shifts in setting angle, with the two halves of the branched chain often at different values. On the other hand, Fig. 13(b) shows the setting angles for all of the chains in the system, now averaged over all of the 3MS in each chain. The colour maps indicate a significant degree of chain rotation, consistent with the classification as a rotator phase. It also indicates another particularly interesting feature.

The chain-average setting angle map for chain 10 presents a colour trace that contains a lot of dark grey. Each dark point in the trace indicates that none of the 3MS in the chain is aligned to the chain axis and so there are no 3MS setting-angles defined for the chain at that point in the simulation. This is shown in more detail in Fig. 14. This reveals that the chain is in a highly kinked state, containing many persistent *gauche* defects, and then only for part of the time. Only one other chain in the system, number 33, contains a large proportion of *gauche* defects. In fact, most of the others contain a small proportion of *gauche* defects, while two (chains 3 and 11) are all-*trans*, for the duration of the production run.

The contracted, or collapsed, conformation of chain 10 is an exceptional type of behaviour in these branched chain simulations. However, we have found that it appears routinely in simulations of rotator phases at high pressure and temperature, and this will be discussed in a forthcoming publication [41].

4.5. Setting angle correlations

Correlation functions were calculated between the 3MS setting angles separated by various distances along the molecular backbone. These ‘intra-chain’ correlation functions are shown in Fig. 15 for the finite chain models. For the low branch content systems, up to 2.6 SCB/1000C, the correlations appear very similar, and drop off rapidly with distance along the chain. However, when the branch content is increased further to 5.21 and 10.4 SCB/1000C, there is a clear increase in the correlation along the chain. Once the branch concentration is doubled again—by shortening the chains—the simulation enters a mobile phase, and the correlation along the chains is further strengthened: the chains have an increased rigidity,

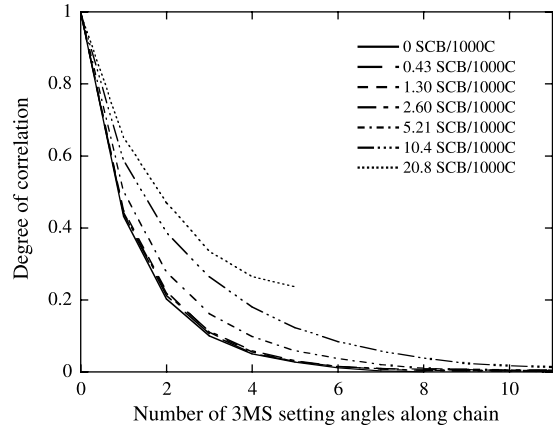

Fig. 15. The linear intra-chain angular correlation between 3MS setting angles for the finite chain models. The 20.8 SCB/1000C trace stops at 5×3MS segments, because of the shorter chain repeat in this model.

and their motion begins to resemble that of a rigid rotor. A more extreme example of this type of correlation has been observed in high pressure rotator phases (see [41]).

We examine the correlations between setting angles of 3MS's on adjacent chains by plotting setting angle difference distributions (Fig. 16). These indicate the most likely relative orientations of adjacent neighbours in the [110] direction. Thus, for herringbone packing, the first nearest neighbour distribution should contain a peak at 90°, while the second nearest neighbour distribution should be peaked at 0 and 180°. This is indeed the pattern we observe, up to 5.21 SCB/1000C. However, for the more highly branched systems, the behaviour alters.

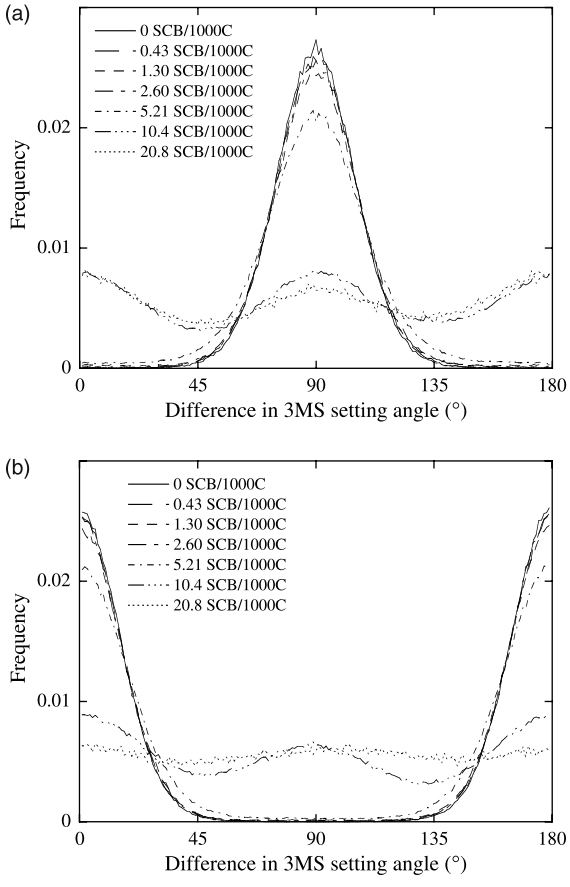

Fig. 16. The distribution of setting angle differences between a 3MS and (a) the first nearest and (b) the second nearest neighbour 3MS in the [110] direction for the finite chain models.

The 10.4 SCB/1000C system has peaks at 0 and 90°, in both the first and second nearest neighbour distributions. In fact, although it is not shown here, this behaviour persists up to the fourth nearest neighbour. The implication is that the system is maintaining long-range orientational order, but that parallel arrangements of the chains are as common as herringbone packing. For the system with 20.8 SCB/1000C, a similar effect is observed in the first nearest neighbour distribution, but the second nearest neighbour (and also that of the more distant neighbours) is relatively flat. Therefore it is clear that this system possesses only short-range orientational order, a finding which is entirely consistent with our designation of the phase as a rotator phase.

5. Discussion

A number of interesting observations may be made concerning the results presented here. In the first place, it is clear that the inclusion of branches within the crystalline unit cell leads to lattice expansion. However, it is difficult to draw quantitative comparisons between simulation and experiment, for two reasons. Firstly, it is not clear, in most cases, what proportion of the branches in a semicrystalline polymer are to be found within the crystals, and secondly, the rejection of branches to the surfaces of the crystals will inevitably lead to a reduction in lamellar thickness that can also be related to an expansion in a and b. The latter effect is not accounted for at all in our modelling.

The true crystalline branch content is rarely quoted in the literature, as it requires quite subtle NMR measurements. However, we have found one material in the literature, for which both X-ray diffraction measurements and NMR analyses are available and whose behaviour is consistent with the simulated findings (see Fig. 4). The other available experimental data displays similar qualitative trends in the lattice parameters, but as a function of total branch content. The data of Howard and Crist [13] is particularly interesting because the lattice expansion shows a plateau at large branch contents, which might be interpreted as meaning that there is an upper limit to the crystalline branch content. The plateau occurs at a lattice expansion corresponding to a crystalline branch content of 3 SCB/1000C. However, Pérez et al. [22] have measured a crystalline branch content of 6 SCB/1000C in another ethyl-branched sample, so there may be other factors, such as crystallisation temperature, which play a role. To the best of our knowledge, there have been no reports in the literature of crystalline branch contents above 10 SCB/1000C, so it seems likely that our simulations of 10.4 and 20.8 SCB/1000C are unrealistic. Nevertheless, the discovery of a mobile rotator phase at the highest branch content simulated is interesting and warrants further discussion. First, however, it is worth

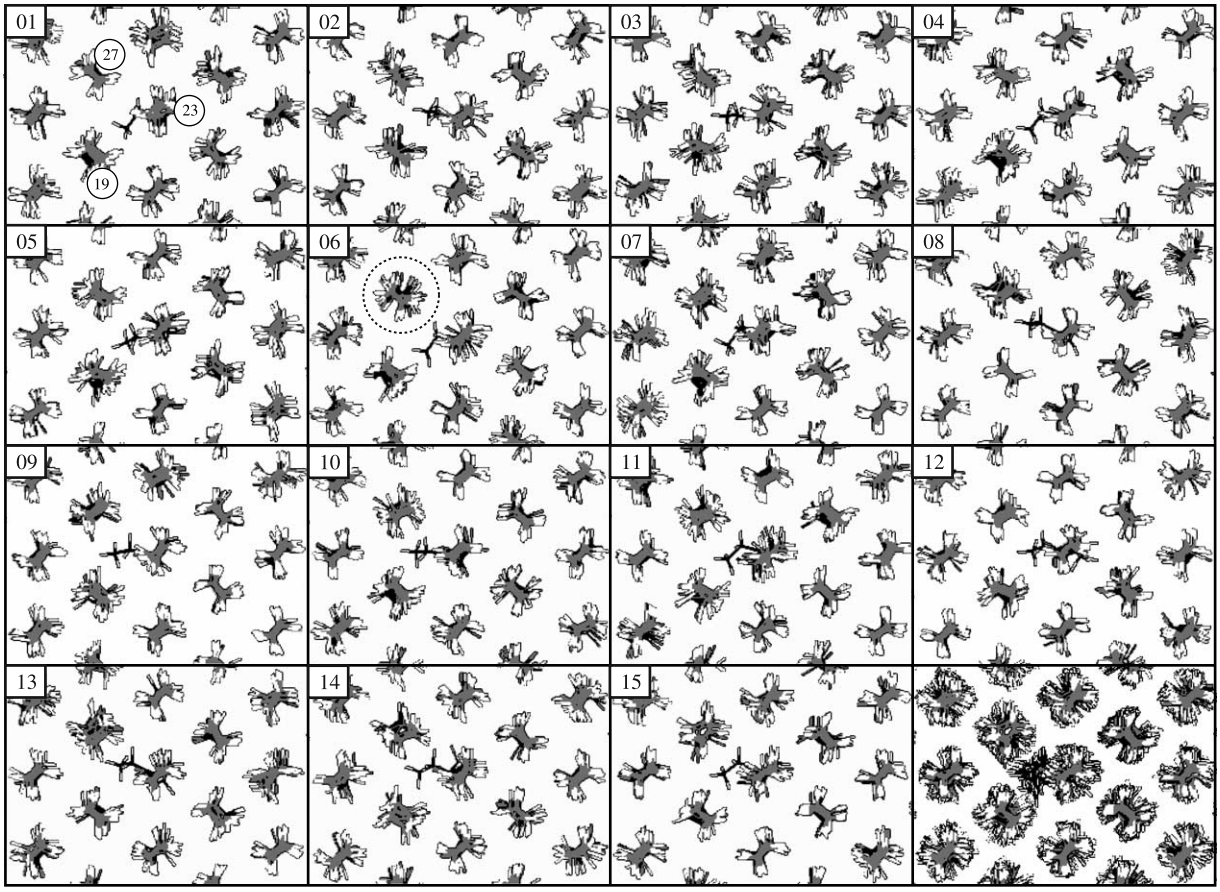

Fig. 17. Fifteen snapshots, taken at 1 ps intervals during a simulation of the $4\times6\times12$ model containing a single branch, together with (bottom right) a superposition of all fifteen frames.

considering further the issue of exactly how the ethyl chain branch is accommodated in the unit cell.

Fig. 17 shows 15 snapshots taken at 1 ps intervals during a simulation of a $4\times6\times C_{24}$ infinite chain model containing a single branch. Only the central region of the simulation box is shown, with three of the chains (19, 23 and 27) marked. The branch is attached to chain 23, at point q, as discussed in the Methods section (see Fig. 2). It can be seen, however, that the terminal methyl group explores quite a large region of space between chains 23, 27 and 19, adopting conformations in which the C–C bond of the ethyl branch is sometimes close to being parallel to the backbone (as close as the bond geometry will allow) but often nearer to being perpendicular, as suggested by Napolitano et al. [23]. The volume of space swept out by the branch is visualized in the final frame of Fig. 17 (bottom right) in which all 15 snapshots have been superimposed.

In order to accommodate the branch within the structure, it is necessary for the other chains to distort, and it is clear that this must be a dynamic process, with the backbones continually readjusting their conformations to allow for the motions of the branch. It is also clear, from a close inspection of the final frame of Fig. 17, that most of the distortion occurs in the triad of chains immediately surrounding the branch; in the more distant chains, the projections of the planar zig-zags are still clearly visible, indicating a lack of movement on their part.

Fig. 17 shows another interesting effect, not previously noted. Chain 27 actually undergoes a 90° rotation, from herringbone to parallel alignment. The rotation occurs during frame 6, in which it can be seen that the chain appears more than usually twisted. This type of chain rotation is not normally observed in unbranched infinite systems of this size at 300 K [24], and so we must attribute it to the presence of the branch. However, it seems likely that this behaviour is also a consequence of the short repeat length of the chains, which limits the ability of the chains to relieve strain by conformational changes alone.

It has previously been speculated that the incorporation of chain branches in PE crystals require the presence of specific types of defect. For example, several workers have suggested that a g^+tg^- (or $2g1$) defect would be one way of relieving the strain around each branch [42–46]. In fact, energy calculations and mechanical measurements have already shown the density of such defects to be far too low to account for all of the branches known to be present [47]. However, the maps of torsions and setting angles presented above give us the opportunity to search for other defect structures that may be associated with branches.

The most striking finding is that branch points do not generally lead to the formation of *gauche* defects. The clearest defect structure found occurs in the infinite chain simulation. There, throughout the simulation, chain 27 i.e. the chain

adjacent to the branched one (see Fig. 9(b)), displays a distorted triplet of 3MS's. In this triplet, we observe one torsion distorted towards the *trans-gauche*$^+$ barrier, one similarly distorted towards the *trans-gauche*$^-$ barrier, and between them a *trans* 3MS which is, however, tilted away from the chain axis. This structure is actually a nascent $2g1$ or g^+tg^- defect, and does occasionally resolve into such a defect for brief periods up to about a picosecond. This is the closest structure that we observe to that predicted in Refs. [42–46], and in fact, it only occurs in the infinite chain models. Although g^+tg^- defects *are* occasionally found in the finite chain models, they are not specifically associated with branches. Instead we only find very slight torsional distortions in the finite chain systems, from which we conclude that most strain in these systems is relieved through rigid displacements of the chains, with occasional twist defects (such as that shown in chain 26, Fig. 11(b)) in which one chain appears to rotate around the branch on its neighbour.

The 90° flip observed in Fig. 17 is one of only two that were observed during the infinite chain simulations. The other was also observed in the branched $4\times6\times12$ model, and was again adjacent to the branch. In general however, the herringbone arrangement, taken as the starting configuration for all simulations, appears to be stable for the duration of both the equilibration and sampling periods, for all models with branch contents up to 5.21 SCB/1000C. For these models, no other 90° flips were observed, apart from those already noted. On the other hand, the 10.4 SCB/1000C simulations show the formation of a parallel domain, which appears to coexist in a dynamic equilibrium with the herringbone domain. However, the majority of the rotations occur during the equilibration phase of the simulation, aided by the volume fluctuations that occur when using the isobaric–isothermal ensemble. In fact the 10.4 SCB/1000C model displays only a single 90° chain rotation during the 50 ps equilibration period, although large amplitude librations ($\pm30°$) are common.

The most unusual finding from our simulations is the occurrence of a mobile rotator phase at the highest branch concentration (20.8 SCB/1000C). The phase is characterised by short range orientational order, coupled with long range positional order in the *a*–*b* plane, frequent large amplitude rotations during both the equilibration and sampling phases of the simulation, and chain sliding parallel to *c*. The ratio *a*/*b* is less than but close to $\sqrt{3}$, which is generally regarded as necessary for the formation of mobile phases. While such a phase has never been reported experimentally, it is nevertheless instructive to consider how it arises.

The principle driving force for the formation of the mobile phase would appear to be the lattice expansion resulting from the inclusion of the branches.

Because the branches are relatively localised along the chains, there will be regions with excess free volume, in which chain rotations will occur more readily. It is noteworthy that the rotator phase is only observed in the shorter finite chain simulation. An inspection of the intrachain angular correlation function (Fig. 15) indicates that the chains in this simulation behave more rigidly than in the longer chain simulations—a consequence of the periodic nature of the simulation box which was discussed above—and this may contribute to the formation of this unusual phase.

The possibility of a mobile phase, induced by the expansion of the lattice parameters, is intriguing, because of its possible ramifications for polymer crystallisation. The mobile phase described in this paper exhibits many of the features required in the proposed size dependent transient phase of Keller et al. [48], and the implication of our simulations is that short chain branches will encourage the formation of such a phase.

Another interesting possibility is that the branched chain mobile-phase could provide a mechanism for branch exclusion from the crystals. Where there is a high density of branches in a lattice, chain sliding is increasingly possible, with the result that the branches are more readily transported to regions where there is more free-volume, such as an interfacial region or the amorphous surround. This speculative mechanism could help to account for the observed upper limit of branch content within polymer crystals.

The simulations presented in this paper are limited, as all computer simulations of PE crystals are, by the size of system that can be handled by the current generation of computers. It is clear that some of the effects discussed here are dependent on model size; for example, it is clear that the $4\times6\times12$ models are overly constrained conformationally, compared with real systems. We might hope to improve the realism of our simulations in the future by considering ever larger models, and we might also make use of improvements in computing resources to use multiple starting configurations, to try to avoid any possibilities of bias due to a particular arrangement of the chain branches. Nevertheless, despite their small sizes, the simulations presented here offer useful and interesting insights into the behaviour of the chain branches within crystals of short-chain-branched polyethylenes.

6. Conclusions

Molecular dynamics simulations have been used to investigate possible mechanisms for $-C_2H_5$ branch inclusion in crystals of PE. Computer models based on both finite *n*-alkanes and infinite, periodically bonded, polymers have been considered, with branch densities in the range 0 to 20.8 SCB/1000C. All the simulations were performed at 300 K and ambient pressure-equilibration was performed using the isobaric–isothermal ensemble, and sampling employed the microcanonical ensemble. The general observation was that increasing the number of branches included within the crystals led to a gradual expansion of the unit cell parameters, principally in the *a* direction. An examination of the polymer backbones close to the chain branches failed to identify any regular defect structure associated with the branches. It would appear that any strain arising from the incorporation of ethyl branches into the crystal is relieved by gradual conformational changes spread over many monomers within each backbone. The ethyl branch appears to spend a significant fraction of the simulation in conformations, which are perpendicular to the chain axis. This occurs via a dynamic rearrangement of the three chains closest to the branch i.e. the branched chain itself

and the two nearest neighbours adjacent to the branch. The g^+tg^- ($2g1$) defect combination was found to occur only in the infinite chain simulations, and then the *gauche* states were not fully developed for the majority of the simulation time. We describe this state as a *nascent* g^+tg^- defect and, in agreement with previous workers [47], conclude that it does not play a major role in the incorporation of branches.

At the highest level of branching sliding of the chains was observed, and a mobile rotator phase was formed. The onset of chain sliding appears to result, under ambient conditions, from the expansion of the lattice parameters due to the presence of branched chains. While this phase has not been observed experimentally, the possibility of such a phase has interesting implications for the mechanism by which partitioning of the short-chain branches occurs, between the crystalline and amorphous phases during crystallisation.

Acknowledgements

The authors wish to thank the Engineering and Physical Sciences Research Council of the UK and the H. H. Wills Physics Department, University of Bristol, for supporting this project through a Ph.D. studentship. They are grateful to Dr A. E. Terry, Dr J. K. Hobbs and Dr P. J. Barham for long and helpful discussions concerning the experimental behaviour of PE and the long *n*-alkanes, and to Prof. M. P. Allen and Prof. J. H. R. Clarke for advice on computational techniques. They are particularly grateful to Dr Anne Baker for sharing details of her results with them at an early stage.

References

[1] Gornick F, Mandelkern L. Effect of noncrystallizable components on crystallization kinetics of polymers. J Appl Phys 1962;33:907–13.
[2] Helfand E, Lauritzen JI. Theory of copolymer crystallization. Macromolecules 1973;6:631–8.
[3] Eichhorn RM. Unit cell expansion in polyethylene. J Polym Sci 1958;31:197–8.
[4] Walter ER, Reding FP. The appearance of a new crystalline phase in stretched, linear polyethylene. J Polym Sci 1956;21:557–9.
[5] Cole EA, Holmes DR. Crystal lattice parameters and the thermal expansion of linear paraffin hydrocarbons, including polyethylenes. J Polym Sci 1960;46:245–56.
[6] Swan PR. Polyethylene unit cell variations with branching. J Polym Sci 1962;56:409–16.
[7] Wunderlich B, Poland D. Thermodynamics of crystalline linear high polymers. 2. Influence of copolymer units on thermodynamic properties of polyethylene. J Polym Sci, Part A: General 1963;1:357–72.
[8] Richardson MJ, Flory PJ, Jackson JB. Crystallization and melting of copolymers of polymethylene. Polymer 1963;4:221–36.
[9] Bodily D, Wunderlich B. Thermodynamics of crystalline linear high polymers. 4. Effect of ethyl acetate and hydroxyl side groups on properties of polyethylene. J Polym Sci, Part A-2: Polym Phys 1966;4:25–40.
[10] Baker CH, Mandelkern L. Polymer 1966;7:71–83.
[11] Kavesh S, Schultz JM. Lamellar and interlamellar structure in meltcrystallized polyethylene. 1. Degree of crystallinity, atomic positions, particle size, and lattice disorder of first and second kinds. J Polym Sci, Part A-2: Polym Phys 1970;8:243–76.
[12] Preedy JE. A study of branching in ethylene copolymers by X-ray diffraction. Br Polym J 1973;5:13–19.
[13] Howard PR, Crist B. Unit-cell dimensions in model ethylene butene-1 copolymers. J Polym Sci, Part B: Polym Phys 1989;27:2269–82.
[14] Bunn CW. Molecular structure. In: Renfrew A, Morgan P, editors. Polythene: the technology and uses of ethylene polymers. London: Iliffe; 1957. p. 81–120.
[15] Davis GT, Eby RK, Martin GM. Variations of unit-cell dimensions of polyethylene—effect of crystallization conditions annealing deformation. J Appl Phys 1968;39:4973–81.
[16] Davis GT, Eby RK, Colson JP. Thermal expansion of polyethylene unit cell: effect of lamella thickness. J Appl Phys 1970;41:4316–26.
[17] Baker AME, Windle AH. An X-ray diffraction and modelling study of short chain branch location within the structure of polyethylene. Polymer 2001;42:681–98.
[18] Kitamaru R. Phase structure of polyethylene and other crystalline polymers by solid-state ^{13}C NMR. Adv Polym Sci 1998;137:41–102.
[19] Alamo RG, Mandelkern L. The crystallization behavior of random copolymers of ethylene. Thermochim Acta 1994;238:155–201.
[20] Russell KE, Wu G, Blake S, Keyding RD. ^{13}C NMR and X-ray diffraction studies of the morphology of alkanes and linear polyethylenes. Polymer 1992;33:951–7.
[21] Pérez E, VanderHart DL, Crist B, Howard PR. Morphological partitioning of ethyl branches in polyethylene by ^{13}C nuclear-magnetic-resonance. Macromolecules 1987;20:78–87.
[22] Pérez E, Bello A, Perena JM, Benavente R, Martinez MC, Aguilar C. Solid-state nuclear-magnetic-resonance study of linear low-density polyethylenes. 1. Ethylene–1-butene copolymers. Polymer 1989;30:1508–12.
[23] Napolitano R, Pucciariello R, Villani V. Conformational and packing energy calculations on ethylene copolymers. Macromol Theory Simul 1994;3:623–32.
[24] Phillips TL, Hanna S. A comparison of computer models for the simulation of crystalline polyethylene and the long *n*-alkanes. Polymer. in press, doi: 10.1016/j.polymer.2005.09.040.
[25] Ryckaert JP. On the simulation of plastic crystals of *n*-alkanes with an atomistic model. Physica A 1995;213:50–60.
[26] Bunn CW. The crystal structure of long-chain normal paraffin hydrocarbons. The 'shape' of the CH_2 group. Trans Faraday Soc 1939;35:482–91.
[27] Farmer BL, Eby RK. Methyl branches in hydrocarbon crystals—calculation of relaxation effects. J Appl Phys 1974;45:4229–38.
[28] Farmer BL, Eby RK. Energetics of methyl branches in hydrocarbon crystals. Polymer 1979;20:363–6.
[29] Smith W, Forester TR. DL-POLY-2.0—a general-purpose parallel molecular-dynamics simulation package. J Mol Graph 1996;14:136–41.
[30] Berendsen HJC, Postma JPM, van Gunsteren WF, DiNola A, Haak JR. Molecular dynamics with coupling to an external bath. J Chem Phys 1984;81:3684–90.
[31] Nosé S. A unified formulation of the constant temperature molecular dynamics methods. J Chem Phys 1984;81:511–9.
[32] Hoover WG. Canonical dynamics equilibrium phase space distribution. Phys Rev A 1985;31:1695–7.
[33] Ryckaert JP. Special geometrical constraints in the molecular-dynamics of chain molecules. Mol Phys 1985;55:549–56.
[34] Smith GD, Yoon DY. Equilibrium and dynamic properities of polymethylene melts from molecular dynamics simulations. I. *n*-tridecane. J Chem Phys 1994;100:649–58.
[35] Allen MP, Tildesley DJ. Computer simulation of liquids. Oxford: Oxford Science Publications; 1987.
[36] Doherty DC, Hopfinger AJ. Molecular modeling of polymers: molecular dynamics simulation of the rotator phase of $C_{21}H_{44}$. Phys Rev Lett 1994;72:661–4.
[37] Sirota EB, King HE, Singer DM, Shao HH. Rotator phases of the normal alkanes: an X-ray scattering study. J Chem Phys 1993;98:5809–24.
[38] Geil PH, Anderson FR, Wunderlich B, Arakawa TJ. Morphology of polyethylene crystallized from the melt under pressure. J Polym Sci A 1964;2:3707–20.
[39] Bassett DC, Block S, Piermarini GJ. A high-pressure phase of polyethylene and chain-extended growth. J Appl Phys 1974;45:4146–50.

[40] Bassett DC, Turner B. On the phenomenology of chain extended crystallization in polyethylene. Phil Mag 1974;29:925–55.
[41] Phillips TL, Hanna S. Simulations of the mobile phases of polyethylene. in press, doi:10.1016/j.polymer.2005.09.019.
[42] Pechhold W. Molecular mobility in polymers. 1. Concept of a solid state physics of macromolecular structures. Kolloid ZZ Polym 1968; 228:1–38.
[43] Scherr H, Pechhold W, Blasenbrey S. Molecular movement in polymers. 2. Force dipoles, volume effect and relaxation behavior of 2*gl*-kink in pe-crystal. Kolloid ZZ Polym 1970;238:396–405.
[44] Martinez de Salazar J, Baltá-Calleja FJ. Influence of chain defects on the crystallization of polyethylene with reference to crystal size and perfection. J Cryst Growth 1979;48:283–94.
[45] Baltá-Calleja FJ, Hosemann R. Distribution of chain defects and microstructures of melt crystallized polyethylene. II. Influence of defect size and of plastic deformation. J Polym Sci, Polym Phys Ed 1980;18: 1159–65.
[46] Gaucher V, Seguela R. Phase partitioning of the chain defects in ethylene butene copolymers in the framework of the crystalline chain kink model. Polymer 1994;35:2049–55.
[47] Boyd RH. The energetics of kinks in polyethylene. J Polym Sci, Polym Phys Ed 1975;13:2345–55.
[48] Keller A, Hikoska M, Rastogi S, Toda A, Barham PJ, Goldbeck-Wood G. An approach to the formation and growth of new phases with application to polymer crystallization—effect of finite-size, metastability and Ostwald rule of stages. J Mater Sci 1994;29(10):2579–604.